



## Mechanical-thermal coupling fatigue failure of CoCrFeMnNi high entropy alloy



Chaofan Li<sup>a</sup>, Zhichao Ma<sup>a,b,c,\*</sup>, Shuai Tong<sup>a</sup>, Jize Liu<sup>a</sup>, Wei Zhang<sup>a</sup>, Guoxiang Shen<sup>a</sup>, Shenghui Wang<sup>a</sup>, Hongwei Zhao<sup>a,b,c</sup>, Luquan Ren<sup>d,e</sup>

<sup>a</sup> School of Mechanical and Aerospace Engineering, Jilin University, Changchun, 130025, China

<sup>b</sup> Key Laboratory of CNC Equipment Reliability, Ministry of Education, Jilin University, Changchun, 130025, China

<sup>c</sup> Institute of Structured and Architected Materials, Liaoning Academy of Materials, Shenyang, 110167, China

<sup>d</sup> Key Laboratory of Bionic Engineering Ministry of Education, Jilin University, Changchun, 130025, China

<sup>e</sup> Weihai Institute for Bionics-Jilin University, Weihai, 264207, China

### ARTICLE INFO

#### Keywords:

Fatigue  
Mechanical-thermal coupling  
Temperature  
High-entropy alloys  
Microevolution

### ABSTRACT

High entropy alloys exhibit excellent performance under different-temperature conditions. In order to investigate the effect of temperature on the mechanical-thermal coupling fatigue failure of classical CoCrFeMnNi high entropy alloy to accelerate the application of high entropy alloys, the uniaxial tensile and fatigue tests at temperatures ranging from RT to 500 °C were conducted, and statics simulation analysis of fatigue specimens under fatigue loading conditions was conducted. The results of the uniaxial tensile tests illustrated that the yield stress and tensile strength of the alloy decreased with increasing temperature. In contrast, the elongation after the fracture of the alloy increased with temperature. The fatigue test results revealed that the fatigue life decreased as the temperature increased. The fracture morphology of the fatigue specimens and the flank morphology and dislocation distribution near the crack nucleation zone were collected to support the investigation. Accordingly, the reasons for the high-temperature-induced decrease in fatigue crack nucleation and propagation lives were systematically investigated. The main reasons for the higher-temperature-induced decrease in crack nucleation lives were a decrease in the yield stress of the alloy, more easily triggered dislocation motion and stress homogenization. The reasons for the decrease in fatigue crack propagation lives induced by higher temperatures were the more prone occurrence of dislocation motion, a decrease in yield stress, and a decrease in the area of the crack propagation region.

### 1. Introduction

Fatigue failure is one of the most common failure modes of structures or materials [1–4]. Fatigue failure is prone to occur on manned machinery subjected to reciprocating loads, such as aircraft [5], vehicles [6–8], and ships [9]. Additionally, fatigue failure is often sudden and unpredictable [10]. Therefore, fatigue failure poses a severe threat to human safety. Simultaneously, fatigue failure also contributes to critical structural failures, such as in aviation engine blades [5], turbine rods, and axles [11]. Especially for typical service conditions in machinery, the coupled mechanical and thermal service conditions [12] require the preferable performance of materials. Materials and structures under harsh service conditions are subjected to cyclic loads and additional effects caused by higher temperatures, such as softening [13],

dislocation movement and grain boundary migration [14,15], which seriously affect the instability and reliability of materials in service. High entropy alloys exhibit excellent performance under different-temperature conditions [16–18]. Therefore, there is an urgent need to develop high entropy alloys suitable for use under coupled mechanical and thermal fatigue conditions to meet increasingly extreme fatigue service conditions.

In recent years, research on the properties of high entropy alloys, known as the king of future materials, has become a hot topic. Li et al. investigated the sawtooth behavior and shear bands of a CoCrFeMnNi high-entropy alloy under high strain rate deformation conditions [19]. Veeresham et al. established a machine-learning model to predict the yield stress of nitrogen-doped CoCrFeMnNi high entropy alloys at room temperature [20]. Park et al. investigated the microstructure evolution

\* Corresponding author. School of Mechanical and Aerospace Engineering, Jilin University, Changchun, 130025, China.

E-mail address: [zcma@jlu.edu.cn](mailto:zcma@jlu.edu.cn) (Z. Ma).

of a CoCrFeMnNi alloy under two-stage tensile conditions consisting of room temperature pre-tensile and higher temperature tensile [21]. Zheng et al. investigated the recrystallization and grain expansion behavior of CoCrFeMnNi high-entropy alloys with different plastic deformations [22]. Lu et al. studied the balance between the strength and ductility of high-entropy alloys [23]. Jeong et al. investigated the effects of grain size and temperature on the tensile behavior and deformation mechanism of a high-entropy Fe<sub>41</sub>Mn<sub>25</sub>Ni<sub>24</sub>Co<sub>8</sub>Cr<sub>2</sub> alloy [24]. R.B. Figueredo et al. investigated the effect of grain size on the strength and deformation behavior of a CoCrFeMnNi alloy [25]. Most research on CoCrFeMnNi high entropy alloys has focused on mechanical properties and material microstructure evolution. Nevertheless, according to statistics, more than 80% of material failures are attributed to fatigue failure [1–4], and most materials are subjected to fatigue loads. Therefore, several scholars have also studied the fatigue performance and material microstructure evolution of high-entropy alloys. For example, Lam et al. studied the effect of overload on fatigue crack propagation in CoCrFeMnNi high entropy alloys [26]. Rackwitz et al. investigated the effect of grain size on the fatigue performance of high-entropy CrCoNi alloys [27]. Picak et al. investigated the impact of the fine-grained process on the fatigue performance of high-entropy CoCrNiFeMn alloys [28]. An antifatigue high-entropy alloy was designed by Wei et al. through artificial intelligence technology [29]. Lam et al. investigated

the effect of texture caused by tensile overload on the fatigue performance of a CoCrFeMnNi high entropy alloy. Although a few scholars have studied the fatigue performance of high entropy alloys, most of the current research on the fatigue of high entropy alloys has focused only on fatigue at room temperature. Research on the mechanical-thermal coupling fatigue of high entropy alloys with excellent performance could promote the application of high entropy alloys.

A typical high-entropy CoCrFeMnNi alloy was prepared through a high-temperature hot pressing sintering process. The uniaxial tensile tests were conducted at room temperature (RT) to 500 °C. Fatigue tests were conducted using notched fatigue specimens at RT to 500 °C, and statics simulations analysis was performed on the specimens under fatigue loading conditions. Afterward, the crack nucleation region morphology, flank morphology and dislocation distribution of the fractured fatigue specimens were characterized through scanning electron microscopy (SEM), optical microscopy, and electron backscatter diffraction (EBSD), respectively. Finally, based on the characterization of fatigue specimens after fracture and the results of fatigue testing, tensile testing, and finite element analysis, the influence of temperature on the fatigue crack nucleation and propagation lives and the reason for this influence were systematically studied.

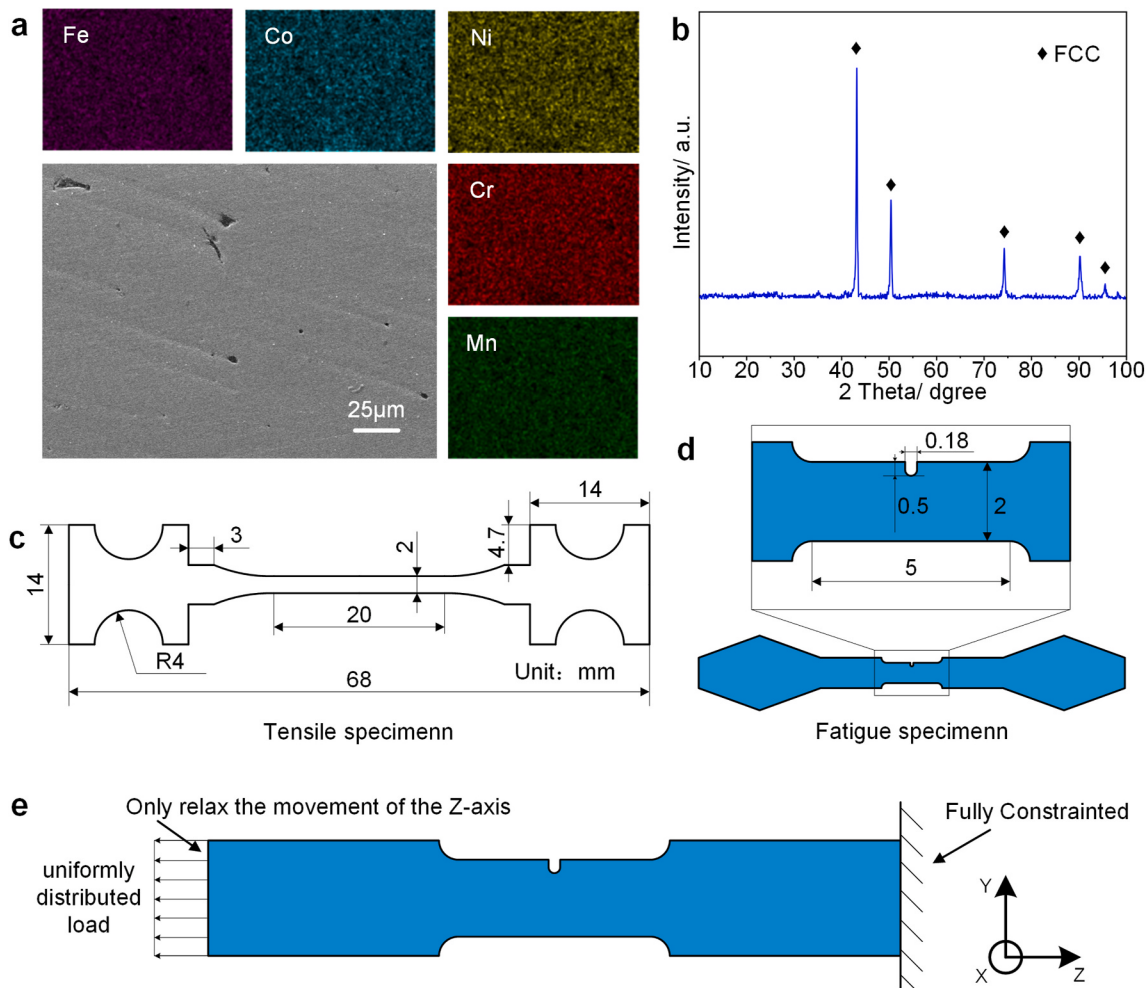


**Fig. 1.** Characterization, dimensions of the CoCrFeMnNi high entropy alloy specimens and constraints of the finite element models, a and b show the results obtained by energy dispersive spectrometer (EDS) and X-ray diffraction (XRD) of the alloy, respectively, c shows the shape and dimensions of the tensile specimen (the thickness was 1 mm, the dimension of the rectangular gauge length:  $l \times b \times t: 20 \times 2 \times 1$  mm), d illustrates the shape and dimensions of the fatigue specimen (the thickness was 1 mm, the dimensions of the rectangular gauge length:  $l \times b \times t: 5 \times 2 \times 1$  mm) with a notch, e shows constraints involved in the finite element analysis of the fatigue specimens.

## 2. Experimental procedure

The CoCrFeMnNi high entropy alloy was prepared by sintering Co, Cr, Fe, Mn, and Ni spherical powders with equal molar ratios into a vacuum hot pressing sintering furnace at a temperature of 1150 °C, a pressure of 20 MPa, and holding for 2 h. The size of the circular cake-shaped material sintered each time was  $d \times h: 70 \times 10$  mm. The results obtained by energy dispersive spectrometer (EDS) and X-ray diffraction (XRD) of the prepared materials are shown in Fig. 1a and b, respectively. Fig. 1a shows that the elemental distribution of the prepared material was primarily uniform, with tiny pores inside the alloy. Fig. 1b shows that the prepared material was a face-centered cubic (FCC) lattice phase. Subsequently, the alloy was prepared into dog bone-shaped plate-shaped tensile specimens and fatigue specimens through wire-cutting technology. The specimens were soaked in acetone and cleaned through ultrasonic cleaning until the surface dirt was removed. Afterward, the specimens were soaked in anhydrous ethanol and cleaned through ultrasonic cleaning for 5 min. The specimens were then taken out and air-dried until their surface was dry. As shown in Fig. 1c, the rectangular gauge length dimension of the tensile specimen was  $20 \times 2 \times 1$  mm. As shown in Fig. 1d, the rectangular gauge length of the fatigue specimen was  $5 \times 2 \times 1$  mm, with a notch at its center with an angle of 0°, a width of 0.18 mm, a depth of 0.5 mm, and a fillet radius of 0.09 mm. The surface roughness of the fatigue specimen was finer than 20 μm.

In order to obtain the different-temperature mechanical properties of the alloy, tensile tests were conducted using a self-developed testing system at ambient temperatures of RT, 340 °C, and 500 °C, with a tensile rate of 1 mm/min. The engineering stress is equal to the axial load of the specimen divided by the cross-sectional area of the gauge section of the specimen. The engineering strain was calculated using a strain correction algorithm [30] based on the displacement between fixtures as input. However, the modulus (from 5.2 GPa to 11.2 GPa) calculated only by the strain correction algorithm [30] differed significantly from the modulus (from 164.97 GPa to 202.90 GPa) of the FeCoNiCrMn alloy in other studies [31], which might indicate that the displacement collected in this study included the displacement of certain elastomers in the instrument. Therefore, it was necessary to deduct the displacement of the instrument from the measured displacement to obtain the displacement of the specimen. The original displacement-force curve obtained from the test conformed to the form of power-law hardening law, as shown in Equation (1):

$$\begin{cases} F_{or} = K_{or}d_{or} & (F_{or} < F_{or}^y) \\ F_{or} = F_{or}^y + R_{or}(d_{or} - d_{or}^y)^{n_{or}} & (F_{or} > F_{or}^y) \end{cases} \quad (1)$$

where  $F_{or}$  and  $d_{or}$  denoted the load and displacement of the measured original load-displacement curve,  $F_{or}^y$  and  $d_{or}^y$  denoted the load and displacement corresponding to yield stress,  $K_{or}$  denoted the stiffness corresponding to the elastic segment of the original curve, and  $R_{or}$  and  $n_{or}$  denoted the hardening coefficient and hardening index corresponding to the plastic segment of the original curve, respectively. The displacement of the original curve consisted of the displacement of the specimen and the displacement of the instrument, as shown in Equation (2):

$$\begin{cases} \frac{F_{or}}{K_{or}} = \frac{F_{or}}{K_{in}} + \frac{F_{or}}{K_{sp}} & (F_{or} < F_{or}^y) \\ \sqrt[n_{or}]{\frac{F_{or} - F_{or}^y}{R_{or}}} + d_{or}^y = \frac{F_{or}}{K_{in}} + d_{sp} & (F_{or} > F_{or}^y) \end{cases} \quad (2)$$

where  $K_{in}$  denoted the stiffness of the instrument,  $K_{sp}$  denoted the stiffness of the specimen, which could be calculated based on the modulus of the specimens, and  $d_{sp}$  denoted the corrected displacement of the specimen. Assuming that elastic modulus of CoCrFeMnNi in this study was

the same as that in the literature [31], explicit expressions for instrument stiffness and specimen displacement correction could be obtained based on Equation (2). Subsequently, based on the corrected load-displacement curve and strain correction algorithm for the specimen, the engineering stress-strain curve of the specimen could be obtained. The clamping method of the specimen and the arrangement of the heating module were described in our previous research [32]. To investigate the effect of temperature on the fatigue performance of the alloy, fatigue tests were conducted at the highest ambient temperatures of RT, 100 °C, 200 °C, 300 °C, 400 °C, and 500 °C, with a constant sinusoidal cyclic load of 76–380 N and a loading frequency of 10 Hz. The testing system used was described in our previous research [33]. The test was repeated 10 times at each temperature to ensure accuracy. Due to the temperature gradient in the axial direction of the specimen, the notch on the fatigue specimen could ensure the same temperature at the crack propagation region of different specimens at the same environmental temperature and relatively regular crack propagation [33]. A static simulation analysis based on Abaqus 2022 was conducted for specimens under fatigue testing conditions. Considering the significant difference in stiffness between the fatigue specimen and the testing instrument, the lateral deformation of the testing instrument could be ignored [33]. Therefore, the geometric model of the fatigue specimen without a clamping section was used for analysis, as shown in Fig. 1e. One end of the geometric model was fully constrained, while the other segment was constrained to retain only the degrees of freedom for the z-axis movement, and a stress load of 127 MPa (calculated by dividing the maximum fatigue load 380 N by the cross-sectional area 3 mm<sup>2</sup>) was applied along the Z-axis direction on the other end of the segment. The material constitutive model used for analysis was the power-law hardening law. The detailed calculation methods and steps for the parameters of the constitutive model would be discussed in the Results and Discussion section. The mesh type used for simulation analysis was a hexahedral mesh, with a mesh size of 0.1 mm. Subsequently, the fracture surface morphology of the fractured fatigue specimens was collected through optical microscopy, and the morphology near the nucleation zone of the fatigue fracture surface at RT and 500 °C, was collected using the scanning electron microscope (SEM). Finally, to analyse the effects of temperature and fatigue loading on the microstructure evolution and crystal orientation of the alloy, electron backscatter diffraction (EBSD) was used to scan the flanks of the specimens near the notch at room temperature and at 500 °C.

## 3. Results and Discussion

The parameters involved in correcting the stress-strain curve are shown in Table 1. Fig. 2a and b shows the corrected engineering stress-strain curves and the mechanical properties of the alloy. Fig. 2a shows that the yield stress decreased from 317 MPa at RT to 158 MPa at 500 °C, similar to previous research results [34]. As the temperature increased, the percentage elongation after fracture increased. Fig. 2b shows that the modulus of the alloy decreased from 203 GPa at RT to 165 GPa at 500 °C, and the tensile strength decreased from 626 MPa at RT to 212 MPa at 500 °C. Although the yield stress under RT was slightly higher than that under 340 °C, it could not be considered that the yield stress under RT was lower than that under 340 °C. Such minor differences might be caused by uneven zeroing of the force sensors. In addition, the differences in pores inside the material caused by sintering could also lead to changes in the macroscopic mechanical properties of the specimens. Alloys would fatigue fail under cyclic loading. The fatigue life of alloys is a vital index for evaluating fatigue performance [35]. As shown in Fig. 2c, under a constant cyclic load of 76–380 N, the fatigue life of the fatigue specimen decreased from  $16.7 \times 10^4$  ( $\pm 2.0 \times 10^4$ ) at RT to  $6.7 \times 10^4$  ( $\pm 0.8 \times 10^4$ ) at 500 °C. The fatigue life comprises the crack nucleation and propagation life [36]. The number of loading cycles from the beginning of loading to the initiation of fatigue crack was called the crack nucleation life, and the number of loading cycles from the

**Table 1**

Related parameters of the displacement correction algorithm.

Temperature/°C	$K_{or}/\text{N-mm}^{-1}$	$F_{or}^y/\text{N}$	$d_{or}^y/\text{mm}$	$R_{or}/\text{Mpa}$	$n_{or}/$	$K_{sp}/\text{N-mm}^{-1}$	$K_{in}/\text{N-mm}^{-1}$
20	683.07	634.64	0.927	186.59	0.572	12378.05	722.97
340	578.67	639.16	1.105	169.24	0.553	10855.48	611.26
500	312.47	315.30	1.009	31.57	0.578	10059.24	322.50

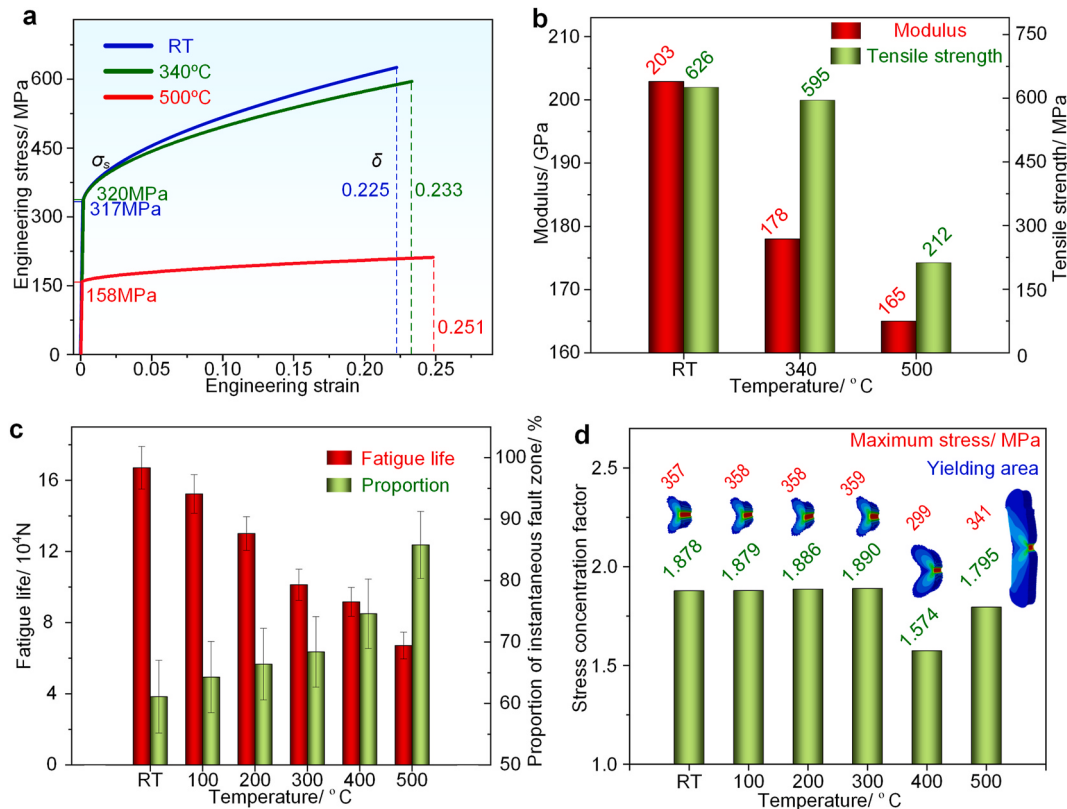


**Fig. 2.** Effect of temperature on the properties and stress concentration coefficient of CoCrFeMnNi high-entropy alloy, a shows the engineering stress-strain curve, b is the temperature-modulus and tensile strength figure, c is the temperature-fatigue life and ratio of the instantaneous fracture region on the fatigue fracture surface figure, and d shows the variation in the stress concentration coefficient and yield region calculated by finite element analysis with increasing temperature.

formation of fatigue cracks to instantaneous fracture was called the crack propagation life. The previous uniaxial tensile test showed that the yield and tensile strength of the alloy gradually decreased with increasing temperature. Under the same loading conditions, the decrease in yield strength led to the increased occurrence of dislocations and slip, accelerating crack nucleation and propagation [37], and thereby reducing the fatigue life of the alloy [33]. In contrast, a decrease in the tensile strength would probably reduce the crack propagation life by reducing the area of the crack propagation region. Therefore, the decrease in the fatigue life of alloys caused by higher temperatures was directly related to a decrease in the strength of the alloy induced by higher temperatures. The fatigue fracture surface consisted of the instantaneous fracture and the crack propagation region. The proportions of the instantaneous fracture region to the entire fracture surface at different temperatures are shown in Fig. 2c. The proportion of the instantaneous fracture region increased from 61.1% ( $\pm 4.9\%$ ) at RT to 85.8% ( $\pm 5.5\%$ ) at 500 °C. This meant that the area of the crack propagation region decreased with the increasing temperature, thus reducing the crack propagation life.

To analyse the influence of temperature on the area near the notch of the fatigue specimens, based on the statics finite element analysis results, the stress concentration coefficient on the notch was calculated. The stress concentration coefficient was the maximum stress at the bottom of the notch obtained from the simulation divided by the nom-

inal stress under the condition of no notch. The nominal stress was 190 MPa, which was obtained by dividing the maximum loading stress of 380 N by the cross-sectional area of the regular gauge section of  $2 \text{ mm}^2$ . The constitutive model used for finite element simulation analysis was the power-law hardening law model [38,39], as shown in Equation (3):

$$\begin{cases} \sigma = E\varepsilon_e & \sigma \leq \sigma_s \\ \sigma = \sigma_s + R\varepsilon_p^n & \sigma > \sigma_s \end{cases} \quad (3)$$

where  $\sigma$ ,  $\sigma_s$ ,  $\varepsilon_e$ ,  $E$ ,  $R$  and  $n$  denoted the stress, yield stress, elastic strain, plastic strain, elastic modulus, hardening coefficient and hardening index, respectively. The parameters  $R$  and  $n$  at RT, 340 °C, and 500 °C were obtained through fitting based on the engineering stress-strain curves. In contrast, the parameters  $\sigma_s$  and  $E$  could be directly calculated from the curve. Considering the limited number of constitutive model parameter groups obtained through fitting, to reduce errors, the parameters at temperatures in the range of RT to 500 °C were obtained through a linear interpolation method based on the parameters at RT, 340 °C, and 500 °C. The calculated constitutive model parameters at temperatures ranging from RT to 500 °C are shown in Table 2.

Based on the calculated constitutive parameters, the maximum stresses at the bottom of the notch at the temperatures ranging from RT to 500 °C were calculated through finite element analysis to be 357 MPa, 358 MPa, 358 MPa, 359 MPa, 299 MPa, and 341 MPa, respectively. The

**Table 2**

Constitutive model parameters of the alloy at RT to 500 °C.

Temperature/°C	$\sigma_y/\text{MPa}$	$R/\text{MPa}$	$E/\text{GPa}$	n
20	317.32	680.30	202.90	0.527
100	317.88	653.98	196.66	0.522
200	318.58	621.08	188.86	0.515
300	319.28	588.18	181.06	0.508
340	319.58	574.87	178.03	0.505
400	258.86	419.95	173.17	0.526
500	157.65	118.60	164.97	0.562

changing trend of the calculated stress concentration coefficient with increasing temperature is shown in Fig. 2d, and the stress cloud map of the yield region calculated by simulation under different temperature conditions is also shown in the figure. The stress concentration coefficient first decreased and subsequently increased with the increase in temperature, and the area of the yield region increased with the increased temperature. The increase in the stress concentration factor in the static simulation was due to more significant lateral deformation exacerbating the notch tearing effect. However, under actual fatigue loading, the actual deformation of the specimen might be less than that under static mechanical simulation, due to the hardening effect of the strain rate on the alloy. The engineering stress-strain curve in Fig. 2a shows that the higher temperatures or the more significant the yield degree of the alloy resulted in a lower rate of stress change relative to the strain and the trend of stress homogenization and strain differentiation. The decreased strength induced by higher temperatures resulted in more areas in the minimum cross-section of the specimen reaching the yield stage and the increased yield degree under the same loading conditions. Therefore, the increase in temperature could lead to stress homogenization and strain differentiation in adjacent areas of the fatigue specimen [32,33]. The minimum cross-section of the fatigue specimen bore tensile-bending composite stress [35], and the stress gradually increased from the notch to away from the notch at the minimum cross-section of

the specimen. The increased temperature would also weaken the nonuniformity of the bending stress [33]. Ignoring other factors, such as the decrease in strength, the trend of stress homogenization caused by higher temperature might lead to delayed fatigue failure.

To systematically evaluate the effect of temperature on fatigue failure, the flank morphology of the fatigue specimens near the fracture surface at temperatures ranging from RT to 500 °C was collected through optical microscopy, as shown in Fig. 3a. The fatigue crack nucleated from the notch on the right and gradually propagated to the left until the load-bearing cross-section of the specimen was insufficient to withstand the fatigue load and instantaneously fractured. The fracture edge at each temperature consisted of a relatively flat right fracture edge, which was a mark left during the crack propagation stage, and a relatively uneven left edge, which was the impact area of instantaneous fracture. At RT to 200 °C, the fracture edges near the notch of the upper and lower specimens (right area) were almost parallel or exhibited a slight angle. From 200 °C to 500 °C, the angle between the fracture edge near notch  $\alpha$  of the upper and lower specimens (in the right area) gradually increased. The previous finite element analysis results indicated that the yield area of the fatigue specimen increased with increasing temperature. Compared to those under RT conditions, the tearing propagation of fatigue cracks caused by higher temperatures was more pronounced, indicating that higher temperatures resulted in alloy softening and strengthening of plasticity, which was consistent with the decrease in modulus and increase in elongation after fracture of the alloy with increasing temperature, as shown in Fig. 2a. Simultaneously, the axial displacement along the specimen caused by material softening might accelerate the nucleation of potential cracks. The crack nucleation life accounted for the majority of the fatigue life. The phenomenon of the crack nucleation stage could best reveal the mechanism of fatigue life reduction induced by higher temperatures [36]. Therefore, the morphology of the crack nucleation region at RT and 500 °C was collected through SEM, as shown in Fig. 3b and c. More cracks appeared at the crack nucleation region of the fracture near the notch at 500 °C

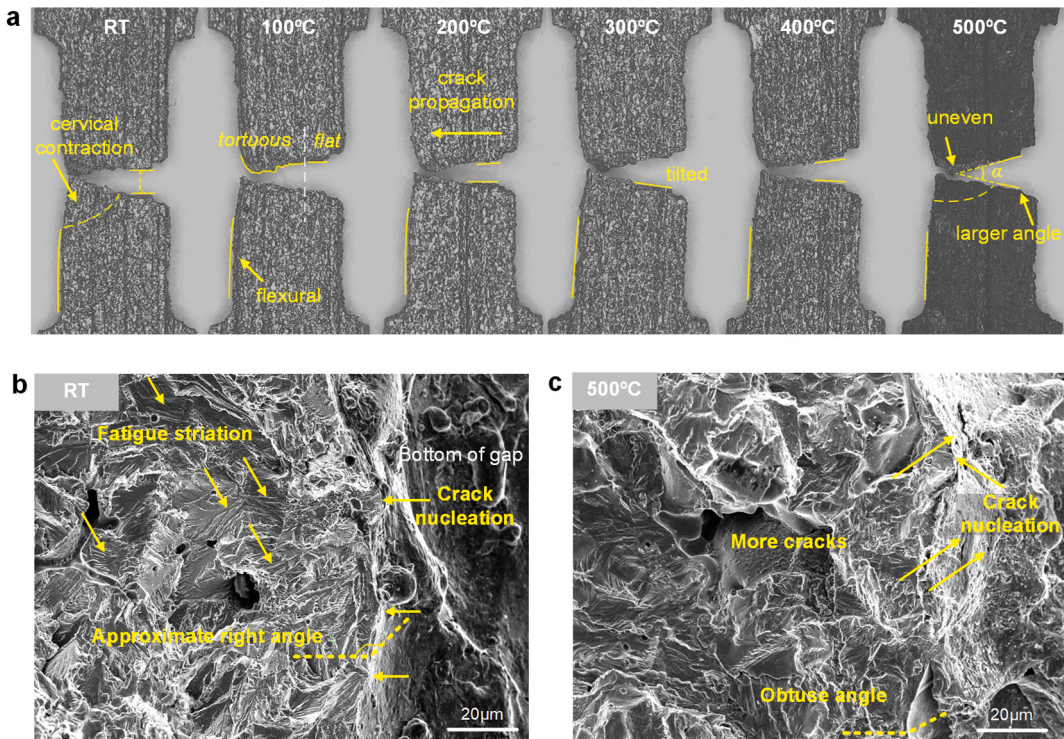


**Fig. 3.** Morphology of the fatigue specimens after fracturing at different temperatures, a shows the morphology of the flank near the fracture surface of the specimens at temperatures in the range of RT–500 °C, b and c show the morphology of the crack nucleation region on the fracture surface at room temperature (RT) and 500 °C, respectively.

than that at RT. Once the first crack formed in the crack nucleation region, stress concentration would occur at the crack tip, and the stress in other areas at the bottom corner of the notch would be partially released. Therefore, the second crack was formed in a lower-stress state under higher-temperature conditions, indicating that crack nucleation was easier under higher-temperature conditions than that under RT conditions, and the same situation was for the main crack. As shown in Fig. 3b, the nucleation point of the crack was concentrated at the protrusion on the right edge of the crack. Both the nucleation point of the crack and the secondary cracks on the surface of the specimen are concentrated at the protrusion at the bottom of the notch, as shown in Fig. 3b. Due to more significant tensile stress, the crack nucleation tendency at the protrusion was stronger [30], so the crack nucleation points were concentrated at the protrusion. In addition, the spacing between the fatigue striations at RT seemed more minor than that at 500 °C, corresponding to the stress homogenization and strength reduction induced by higher temperatures. Simultaneously, wider fatigue striations might correspond to faster crack propagation rates. At RT, the angle between the fracture surface and the bottom of the notch was close to the right angle, while at 500 °C, the angle between the fracture surface and the bottom of the notch was obtuse, indicating that higher temperatures induced more significant plastic deformation at the bottom of the notch and that higher temperatures caused softening and plastic enhancement of the alloy, consistent with the results of tensile testing.

Microstructural characterization of the fractured fatigue specimen flank near the notch at RT and 500 °C was performed via EBSD to comprehensively evaluate the effect of higher temperatures on alloy fatigue failure, as shown in Fig. 4. Kernel average misorientation (KAM) maps at RT and 500 °C are shown in Fig. 4a and b. With regard to the overall distribution of dislocations, the dislocation distribution was more concentrated with a higher dislocation density in the region of concentration at RT than at 500 °C. Except for dislocations near the

fracture surface, dislocations at RT were mainly concentrated on pore defects and some grain boundaries. The dislocations were relatively more dispersed with the lower intensity in the dislocation concentration region at 500 °C than at RT. The concentration of dislocations at 500 °C included defects and almost all grain boundaries, and many dislocations extended to the interior of the grains. The grain boundaries and pore edges were defects, where the atomic distribution was sparser and more uneven than that in the interior of the grain. Therefore, dislocations were more likely to occur at these defects. At 500 °C, with fewer loading cycles, more dislocations expanded into the interior of the grains, indicating that dislocation motion was more easily triggered at higher temperatures than at RT. However, the higher dislocation density intensity in the dislocation concentration region at RT did not necessarily indicate that the dislocation was more prone to aggregation at RT, because the fatigue specimens at RT experienced longer cycling times [26]. In addition, for both RT and 500 °C, the crack edge and the bottom of the notch were the concentration regions of the dislocations. At the bottom of the notch, the influence region of the dislocation at 500 °C was more expansive than that at RT. Higher temperatures could induce stress homogenization in adjacent areas, and stress was the driving force behind dislocation motion. Therefore, a higher temperature resulted in a broader area of dislocation influence at the bottom of the notch. The broader range of dislocations could also cause cracks to appear more randomly at the bottom of the notch, explaining the occurrence of multiple cracks at the notch bottom at 500 °C. Concerning the crack edge, the dislocation density was relatively lower at 500 °C, indicating that only a tiny amount of dislocation motion could propagate fatigue cracks forward under higher-temperature conditions. In summary, higher temperatures promoted the propagation of fatigue cracks in two ways. First, higher temperatures led to easier generation of dislocation motion that drove crack propagation. Additionally, under higher-temperature conditions, the propagation of cracks only required a tiny amount of dislocation motion. In addition, at RT or higher

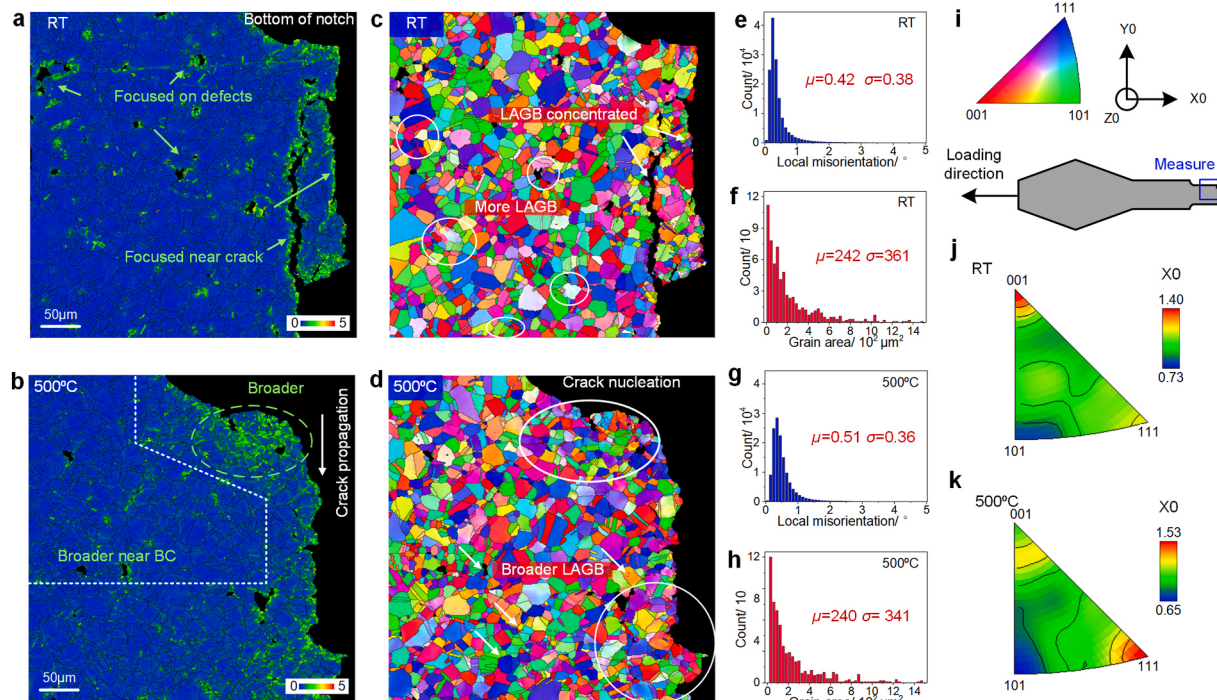


**Fig. 4.** Microstructural characterization obtained from electron backscatter diffraction (EBSD) on the fractured fatigue specimen flank near the notch, a and b show kernel average misorientation (KAM) maps at RT and 500 °C, respectively, c and d show grain orientation and grain boundaries at RT and 500 °C, with red lines representing low angle grain boundaries (LAGBs), e and g show the statistical histograms of the frequency distribution of local misorientation at RT and 500 °C, respectively, f and h illustrate statistical histograms of the frequency distribution of grain area at RT and 500 °C, respectively, i shows the orientation scale of the c and d figures, measurement area, and measurement coordinate axis, j and k are the inverse pole figures along the loading direction at RT and 500 °C, respectively.

temperatures, the dislocation density at the bottom of the notch was more significant than that at the crack edge. The number of cycles before the crack formed stable propagation was relatively more significant, and the region near the notch was loaded multiple times under high-stress conditions. During the crack propagation period, the primary stress concentration area was near the crack tip [33]. Although the crack tip bore enormous stress, the time was relatively short. Finally, from top to bottom, the dislocation density near the fracture surface at 500 °C decreased first and then increased. The initial decrease in dislocation density was attributed to the shorter duration of stress concentration at the crack tip during the crack propagation stage. In contrast, the increase in dislocation density was attributed to the severe plastic deformation of the region affected by instantaneous fracture. Fig. 4c and d shows the grain orientation and grain boundaries on the flank of the fatigue specimen at RT and 500 °C, respectively. The grain orientation at RT and 500 °C was relatively random. The red lines in the figure represent the low-angle grain boundaries (LAGBs). As fatigue loading promoted dislocation motion, the grains would first form LAGBs [40] and even break into large-angle grain boundaries, which was an effort by the alloy to seek fine-grain strengthening to further balance the external forces. The LAGB and refined grains near the bottom of the notch at 500°C were more pronounced than those at room temperature, corresponding to the temperature-induced decrease in alloy strength. In addition, Fig. 4c and d also show that the grains were cracked by small angle grain boundaries near the pore defect, the crack edge, and the area affected by instantaneous fracture. The quantitative analysis of the microstructure is shown in Fig. 4e-f. Fig. 4e, f, 4g, and 4h are frequency statistical histograms of local misorientation at RT, grain area at RT, local misorientation at 500 °C, and grain area at 500 °C, respectively. The mean local misorientation at 500 °C was more significant than that at RT, and the standard deviation of the local misorientation at 500 °C was less than that at RT, which indicated that higher temperatures promoted denser and more evenly distributed dislocations in the fatigue specimens. The mean of grain area at 500 °C was lower than that at RT, and the standard deviation of the grain area at 500 °C was lower than that at RT, which indicated that higher temperatures promoted the fragmentation and homogenization of grains in the fatigue specimens.

Fig. 4j and k shows the inverse pole figures along the loading direction at RT and 500 °C, respectively, and the measured region is shown in Fig. 4i. Fig. 4i also shows the inverse polar coordinates, where the X0 direction was the same as the loading direction of the specimen. At RT, the strength was highest at the grain direction <100> in the reverse pole figure (Fig. 4j), indicating that grains with <100> grain direction similar to the loading direction of the specimen were the most. At 500 °C, the strength was highest at the grain direction <111> in the reverse pole figure (Fig. 4k), indicating that the number of grains with a <111> grain direction similar to the loading direction of the specimen was the highest. Additionally, as previously explained, higher temperatures could promote dislocation motion, and the KAM maps at 500 °C also show a more uniform distribution of dislocation density within grains and at grain boundaries, which might correspond to dislocation motion and grain boundary migration. With regard to the FCC lattice, the (111) crystal plane corresponding to the <111> crystal direction was the densest arrangement surface of the atoms. Therefore, the atomic distribution was the sparsest along the <111> crystal direction. Assuming that the grains rotated during fatigue loading and that the <111> crystal orientation tended to be consistent with the loading direction, the macroscopic behavior of the specimen was that the sample was elongated. Although it could not be determined, it was highly possible that the grains in the fatigue specimen at 500 °C rotated during the loading process, and a grain orientation <111> tended to be consistent with the loading direction.

#### 4. Conclusions

In the present study, the tensile mechanical properties and

mechanical-thermal coupling fatigue properties of CoCrFeMnNi high-entropy alloy were systematically tested. The uniaxial tensile test results showed that the yield stress, and tensile strength decreased with the increase in temperature, while the elongation after fracture increased with increasing temperature. The mechanical-thermal fatigue test results showed that under the same load, the fatigue lives decreased with increasing temperature. The statics simulation analysis under fatigue loading conditions showed that the stress concentration coefficient of the notch of the fatigue specimen first decreased and subsequently increased with increasing temperature, and the yield area of the fatigue specimen increased with increasing temperature. Based on the evolution of the mechanical properties with temperature, finite element analysis results, and analysis of fatigue specimen morphology and dislocation distribution information after fracture, except for more easily triggered dislocation motion at higher temperatures, factors such as the wide range of dislocations near the crack nucleation region, stress homogenization, and strain differentiation caused by higher temperatures accelerated the nucleation of fatigue cracks. The decrease in crack propagation lives caused by higher temperatures was attributed to the increase in crack propagation speed caused by more easily triggered dislocation motion, the decrease in yield stress, and the lower dislocation motion required to promote crack propagation. Simultaneously, the reduced crack propagation region caused by higher temperatures also reduced the crack propagation life.

#### Data availability

The raw/processed data required to reproduce these findings cannot be shared at this time due to technical limitations.

#### Credit authors statement

**Chaofan Li:** Data curation, Formal analysis, Investigation, Writing – original draft. **Zhichao Ma:** Conceptualization, Methodology, Funding acquisition, Writing – review & editing. **Shuai Tong:** Data curation. **Jize Liu:** Project administration. **Wei Zhang:** Materials acquisition. **Guoxiang Shen:** Data curation. **Shenghui Wang:** Project administration. **Hongwei Zhao:** Supervision, Writing – review & editing. **Luquan Ren:** Supervision, Writing – review & editing. All the authors read and approved the manuscript.

#### Declaration of competing interest

The authors declare that they have no known competing financial interests or personal relationships that could have appeared to influence the work reported in this paper.

#### Acknowledgments

This work is funded by the National Natural Science Foundation of China (92266206, 52350039, 52227810), National Key R&D Program of China (2023YFF0716800), Jilin Province Science and Technology Development Plan (20240302065GX) and Jilin Province Creative and Innovative Talents Funding Project (2023RY01).

#### References

- [1] Cular I, Vuckovic K, Glodez S, Tonkovic Z. Computational model for bending fatigue prediction of surface hardened spur gears based on the multilayer method. Int J Fatig 2022;161:106892. <https://doi.org/10.1016/j.ijfatigue.2022.106892>
- [2] An WG, Zhao WT, An H. Reliability analysis of stochastic structural system considering static strength, stiffness and fatigue. Sci China, Ser A G 2022;50(3): 2007. <https://doi.org/10.1007/s11433-007-0035-9>.
- [3] Ma ZC, Li CF, Zhang W, Wang SH, Li JK, Zhao HW, Ren LQ. Modified Coffin-Manson equation to predict the fatigue life of structural materials subjected to mechanical-thermal coupling non-coaxial loading. J Mater Sci Technol 2023;160: 118–27. <https://doi.org/10.1016/j.jmst.2023.03.023>.

- [4] Sim GD, Hwangbo Y, Kim HH, Lee SB, Vlassak JJ. Fatigue of polymer-supported Ag thin films. *Scripta Mater* 2012;66(4):915–8. <https://doi.org/10.1016/j.scriptamat.2012.02.030>.
- [5] Xiong JJ, Zhu YT, Luo CY, Li YS. Fatigue-driven failure criterion for progressive damage modelling and fatigue life prediction of composite structures. *Int J Fatig* 2021;145:106110. <https://doi.org/10.1016/j.ijfatigue.2020.106110>.
- [6] Zhou W, Wang J, Pan ZB, Liu J, Ma LH, Zhou JY, Su YF. Review on optimization design, failure analysis and non-destructive testing of composite hydrogen storage vessel. *Int J Hydrogen Energy* 2022;47(B):38862–83. <https://doi.org/10.1016/j.ijhydene.2022.09.028>.
- [7] You TW, Zhou JS, Gong D, Sun Y, Li BS, Chen JX. Synthesis of random vibration environment spectra for the fatigue analysis and optimization of railway vehicles. *Int J Fatig* 2022;159:106752. <https://doi.org/10.1016/j.ijfatigue.2022.106752>.
- [8] Foti P, Razavi N, Fatemi A, Berto F. Multiaxial fatigue of additively manufactured metallic components: a review of the failure mechanisms and fatigue life prediction methodologies. *Prog Mater Sci* 2023;137:101126. <https://doi.org/10.1016/j.pmatsci.2023.101126>.
- [9] Dong Y, Frangopol DM, Sabatino S. A decision support system for mission-based ship routing considering multiple performance criteria. *Reliab Eng Syst Saf* 2016; 150:190–201. <https://doi.org/10.1016/j.ress.2016.02.002>.
- [10] Tang HQ, Liu LQ. A novel metal-composite joint and its structural performance. *Compos Struct* 2018;206:33–41. <https://doi.org/10.1016/j.compositstruct.2018.07.111>.
- [11] Hou N, Ding N, Qu S, Guo WM, Liu L, Xu N, Tian LA, Xu HX, Chen XF, Zairi F, Wu CML. Failure modes, mechanisms and causes of shafts in mechanical equipment. *Eng Fail Anal* 2022;136:106216. <https://doi.org/10.1016/j.engfailanal.2022.106216>.
- [12] Ma ZC, Du XJ, Zhao HW, Ma XX, Jiang DY, Liu Y, Ren LQ. Note: motor-piezoelectricity coupling driven high temperature fatigue device. *Rev Sci Instrum* 2018;89(1):016102. <https://doi.org/10.1063/1.4998264>.
- [13] Meng G, Gao RL, Liu FH, Yu JX. MoNb<sub>5</sub>, MoNbVTi and MoNbVTiHf multicomponent refractory alloys-Compositional modulated mechanical properties investigating. *Mater Today Commun* 2022;33:104320. <https://doi.org/10.1016/j.mtcomm.2022.104320>.
- [14] Ding B, Ren WL, Zhong YB, Yuan XT, Zheng TX, Shen Z, Guo YF, Li Q, Peng JC, Brnic J, Gao YF, Liaw PK. Revealing the influential mechanism of strain ranges on cyclic-life saturation during creep-fatigue in Nickel-based superalloy DZ445. *Int J Plast* 2022;155:103320. <https://doi.org/10.1016/j.ijplas.2022.103320>.
- [15] Lin YC, Xia YC, Ma XS, Jiang YQ, Chen MS. High-temperature creep behavior of Al-Cu-Mg alloy. *Mat Sci Eng A-Struct* 2012;55:125–30. <https://doi.org/10.1016/j.msea.2012.04.044>.
- [16] Xu T, Chen QJ, Ji L, Wang H, Qu SJ, Feng AH. Thermal stability and oxidation resistance of non-equimolar ratio AlTiVCrNb refractory high-entropy alloys. *Intermetallics* 2023;160:107942. <https://doi.org/10.1016/j.intermet.2023.107942>.
- [17] Dewangan SK, Mangish A, Kumar S, Sharma A, Ahn B, Kumar V. A review on High-Temperature Applicability: a milestone for high entropy alloys. *Eng Sci Technol* 2022;35:101211. <https://doi.org/10.1016/j.jestch.2022.101211>.
- [18] Zhang X, Zhang NN, Xing BW, Yin S. An assessment of the high-temperature oxidation resistance of selected thermal sprayed high entropy alloy coatings. *J Therm Spray Technol* 2022;31(4):1386–403. <https://doi.org/10.1007/s11666-022-01352-w>.
- [19] Li WS, Wang BF, Huang XX, Liu B, Brechtl J, Liaw PK. Mechanical behavior and shear band of a powder-metallurgy-fabricated CoCrFeMnNi high-entropy alloy during high-strain-rate deformation. *J Mater Res Technol* 2022;21:1461–78. <https://doi.org/10.1016/j.jmrt.2022.09.106>.
- [20] Veeresham M, Jain R, Lee U, Park N. Machine learning approach for predicting yield strength of nitrogen-doped CoCrFeMnNi high entropy alloys at selective thermomechanical processing conditions. *J Mater Res Technol* 2023;24:2621–8. <https://doi.org/10.1016/j.jmrt.2023.03.146>.
- [21] Park T, Kim JH. Tensile properties and microstructure evolution during two-stage tensile testing of CoCrFeMnNi high-entropy alloy. *J Mater Res Technol* 2020;9(4): 7551–7. <https://doi.org/10.1016/j.jmrt.2020.05.069>.
- [22] Zheng CW, Wang Y, Jin JS, Gong P, Wang XY, Wen HN, Zhang M. Recrystallization and grain growth behavior of variously deformed CoCrFeMnNi high-entropy alloys: microstructure characterization and modeling. *J Mater Res Technol* 2022; 20:2277–92. <https://doi.org/10.1016/j.jmrt.2022.07.182>.
- [23] Jeong HT, Kim WJ. Grain size and temperature effect on the tensile behavior and deformation mechanisms of non-equiautomic Fe<sub>41</sub>Mn<sub>25</sub>Ni<sub>24</sub>Co<sub>8</sub>Cr<sub>2</sub> high entropy alloy. *J Mater Sci Technol* 2020;42:190–202. <https://doi.org/10.1016/j.jmst.2019.09.034>.
- [24] Cao YK, Zhang WD, Liu B, Liu Y, Du M, Fu A. Phase decomposition behavior and its effects on mechanical properties of TiNbTa<sub>0.5</sub>ZrAl<sub>0.5</sub> refractory high entropy alloy. *J Mater Sci Technol* 2021;66:10–20. <https://doi.org/10.1016/j.jmst.2020.05.038>.
- [25] Figueiredo RB, Wolf W, Langdon TG. Effect of grain size on strength and strain rate sensitivity in the CrMnFeCoNi high-entropy alloy. *J Mater Res Technol* 2022;20: 2358–68. <https://doi.org/10.1016/j.jmrt.2022.07.181>.
- [26] Lam TN, Lee SY, Tsou NT, Chou HS, Lai BH, Chang YJ, Feng R, Kawasaki T, Harjo S, Liaw PK, Yeh AC, Li MJ, Cai RF, Lo SC, Huang EW. Enhancement of fatigue resistance by overload-induced deformation twinning in a CoCrFeMnNi high-entropy alloy. *Acta Mater* 2020;201:412–24. <https://doi.org/10.1016/j.actamat.2020.10.016>.
- [27] Rackwitz J, Yu Q, Yang Y, Laplanche G, George EP, Minor AM, Ritchie RO. Effects of cryogenic temperature and grain size on fatigue-crack propagation in the medium-entropy CrCoNi alloy. *Acta Mater* 2020;200:351–65. <https://doi.org/10.1016/j.actamat.2020.09.021>.
- [28] Picak S, Wegener T, Sajadifar SV, Sobrero C, Richter J, Kim H, Niendorf T, Karaman I. On the low-cycle fatigue response of CoCrNiFeMn high entropy alloy with ultra-fine grain structure. *Acta Mater* 2021;205:116540. <https://doi.org/10.1016/j.actamat.2020.116540>.
- [29] Wei XL, van der Zwaag S, Jia ZX, Wang CC, Xu W. On the use of transfer modeling to design new steels with excellent rotating bending fatigue resistance even in the case of very small calibration datasets. *Acta Mater* 2022;235:118103. <https://doi.org/10.1016/j.actamat.2022.118103>.
- [30] Ma ZC, Zhao HW, Wang KT, Zhou XQ, Hu XL, Lu S, Cheng HB. Note: investigation on the influences of gripping methods on elastic modulus by a miniature tensile device and in situ verification. *Rev Sci Instrum* 2013;84(6):066102. <https://doi.org/10.1063/1.4808374>.
- [31] Laplanche G, Gadaud P, Horst O, Otto F, Eggeler G, George EP. Temperature dependencies of the elastic moduli and thermal expansion coefficient of an equiatomic, single-phase CoCrFeMnNi high-entropy alloy. *J Alloys Compd* 2015; 623:348–53. <https://doi.org/10.1016/j.jallcom.2014.11.061>.
- [32] Tong S, Ma ZC, Sun Y, Li CF, Zhao HW, Ren LQ, Yan CL. Temperature-induced enhancement of tensile strength of perforated Ti-6Al-4V sheet revealed through mechanical-thermal coupling quasi-static tension. *Mat Sci Eng A-Struct* 2022;845: 143235. <https://doi.org/10.1016/j.msea.2022.143235>.
- [33] Li CF, Ma ZC, Zhang W, Tong S, Wang SH, Zhao HW, Ren LQ. Realization of tensile-bending mechanical-thermal coupling fatigue based on a uniaxial tensile-fatigue testing device. *IEEE Trans Instrum Meas* 2022;71:6005709. <https://doi.org/10.1109/TIM.2022.3197793>.
- [34] He JY, Zhu C, Zhou DQ, Liu WH, Nieh TG, Lu ZP. Steady state flow of the FeCoNiCrMn high entropy alloy at elevated temperatures. *Intermetallics* 2014;55: 9–14. <https://doi.org/10.1016/j.intermet.2014.06.015>.
- [35] Li Y, Wei PT, Xiang G, Jia CF, Liu HJ. Gear contact fatigue life prediction based on transfer learning. *Int J Fatig* 2023;173:107686. <https://doi.org/10.1016/j.ijfatigue.2023.107686>.
- [36] Liang Z, Wang XS, Cui YA, Xu W, Zhang Y, He YH. A new data-driven probabilistic fatigue life prediction framework informed by experiments and multiscale simulation. *Int J Fatig* 2023;174:107731. <https://doi.org/10.1016/j.ijfatigue.2023.107731>.
- [37] Han QN, Lei XS, Rui SS, Su Y, Ma XF, Cui HT, Shi HJ. Temperature-dependent fatigue response of a Fe<sub>44</sub>Mn<sub>36</sub>Co<sub>10</sub>Cr<sub>10</sub> high entropy alloy: a coupled in-situ electron microscopy study and crystal plasticity simulation. *Int J Fatig* 2021;151: 106385. <https://doi.org/10.1016/j.ijfatigue.2021.106385>.
- [38] Lu L, Dao M, Kumar P, Ramamurti U, Karniadakis GE, Suresh S. Extraction of mechanical properties of materials through deep learning from instrumented indentation. *P Natl Acad Sci USA* 2020;117(13):7052–62. <https://doi.org/10.1073/pnas.1922210117>.
- [39] Ghanbari SS, Mahmoudi AH. An improvement in data interpretation to estimate residual stresses and mechanical properties using instrumented indentation: a comparison between machine learning and Kriging model. *Eng Appl Artif Intell* 2022;114:105186. <https://doi.org/10.1016/j.engappai.2022.105186>.
- [40] Lu KJ, Chauhan A, Litvinov D, Walter M, Tirunilai AS, Freudenberger J, Kauffmann A, Heilmair M, Aktaa J. High-temperature low cycle fatigue behavior of an equiatomic CoCrFeMnNi high-entropy alloy. *Mat Sci Eng A-Struct* 2020;791: 139781. <https://doi.org/10.1016/j.msea.2020.139781>.